Section 4

Parameterization of atmospheric and surface processes, effects of different physical parameterizations.

Numerical Simulation of Potential Impact of Aerosols on Heavy Rainfall Event Associated with Typhoon Hagibis (2019)

Kentaro Araki[1]

1: Meteorological Research Institute, Tsukuba, Ibaraki, Japan
e-mail: araki@mri-jma.go.jp

1. Introduction

Typhoon Hagibis (2019) caused heavy rainfall in eastern and northern areas in Japan on 11-13 October 2019. The operational mesoscale model of Japan Meteorological Agency (JMA) successfully forecasted the occurrence of the heavy rainfall events, but a quantitative forecast of rainfall amount remains challenges. It is considered that the supply of a large amount of water vapor associated with Hagibis (2019), the front formed on the north side of the typhoon, and the precipitation enhancement due to the orography were important factors for this heavy rainfall (Araki 2020). Aerosols play a key role in not only the earth climate, but also short-term precipitation phenomena, working as cloud condensation nuclei (CCNs) and ice nuclei (INs). Although recent studies have suggested aerosol indirect effects on convective clouds and mesoscale convective systems such as invigoration process by CCNs, uncertainties still remain especially in the aerosol properties of INs and their effects on cloud and precipitation systems. In this study, we investigated the potential impacts of aerosol indirect effects by CCNs and INs on the forecast for the heavy rainfall event associated with typhoon Hagibis (2019).

2. Model settings of sensitivity experiments

Numerical simulations were performed by the JMA <u>N</u>on-<u>H</u>ydrostatic <u>M</u>odel (NHM) with a domain of 2,500 x 2,500 km covering Japan and a horizontal grid spacing of 5 km. The initial and boundary conditions were provided from the 3-hourly JMA mesoscale analysis data and the models were run from 09 JST (JST=UTC+9h) on 11 to 15 JST on 13 October 2019. A convection parameterization scheme was not used and a bulk cloud microphysics scheme with 2-moment cloud water, cloud ice, snow, and graupel was used in a control run (CNTL). As sensitivity experiments on CCNs, experiments with changing a coefficient of number concentration of cloud droplets in the formula of cloud condensation nucleation by factors of 0.1 (CN01) and 10 (CN10) were performed. We also performed experiments with changing coefficients in the formulas of deposition/condensation-freezing-mode ice nucleation (Meyers, 1992) and immersion-freezing-mode ice nucleation (Bigg, 1955) by factors of 0.1 (IN01) and 10 (IN10). Combining these settings, we conducted two sensitivity experiments assuming clean (CIN01) and dirty (CIN10) environments. The other setups in each experiment were the same as those used in Saito et al. (2006).

3. Potential effect of CCNs and INs on a heavy rainfall associated with Hagibis (2019)

Typhoon Hagibis (2019) moved northward over the south of Japan on 11 October, landed in Japan around 19 JST on 12, and moved toward the northeast. Heavy rainfall in eastern and northern areas in Japan began on 11 October and got significant on the north side of the center of the typhoon. Moreover, the precipitation amount particularly increased in the mountainous areas.

Time series of the Regional Specialized Meteorological Center (RSMC) Tokyo best track (BT) central pressure and simulated central pressures are shown in Fig. 1a. The central pressure of each experiment was lower than that of the best track, but the temporal variations were similar. Comparing the central pressures of the sensitivity experiments and the central pressure of CNTL, the absolute values of the differences were more than 1 hPa for CN01 and CIN01 after 12 JST on 12, but both were less than 2.5 hPa (Fig. 1b). In each experiment, the courses of the typhoon were almost the same as the best track while the typhoon passed over land (Fig. 2), and the landing in Japan was delayed by 2 hours.

The radar analysis (RA), results of simulated precipitation in CNTL, and the differences from CNTL for each experiment are shown in Fig. 3. From the comparison with radar analysis, the CNTL successfully reproduced heavy rainfall associated with the typhoon. In the sensitivity experiments, there were the differences of rainfall areas with precipitation amount over 100 mm from CNTL because of the differences of the representations for the location of precipitating clouds including spiral bands associated with typhoon. From the results of sensitivity study on orography in Araki (2020), in addition to the sustained precipitation associated with the front formed in the north side of the typhoon center, orographic precipitation enhancement through the Seeder-Feeder mechanism was suggested to have been important for the heavy rainfall. Although it was expected that the precipitation would also change as the process of precipitation enhancement through the Seeder-Feeder mechanism was modulated in mountainous areas in sensitivity experiments, the present experimental results suggest that the indirect effect of aerosols may affect the overall precipitation associated with both of the typhoon and front. Table 1 shows the summary of central pressures of typhoon at the longitude of 138.7°E and precipitation amounts for RSMC Tokyo best track (radar analysis) and each experiment. Precipitation amounts averaged in all domain were almost the same for each experiment. A comparison of precipitation amounts in the domain A with a particularly large amount of precipitation shows that the averaged precipitation amount in CNTL is almost the same as in RA, and those of the other experiments are almost the same, albeit a few percent different from the CNTL. On the other hand, maximum precipitation in domain A was less in CNTL than in RA, with absolute differences of more than 10% between CN01, IN01, CIN01 and CIN10 compared to the maximum precipitation amount in CNTL.

From these results, it is indicated that the quantitative forecast of maximum precipitation amount is sensitive to the aerosol effect by CCNs and INs. It is desired that the parameterization of CCNs and INs in mesoscale models for the short-term forecast should be improved in the future.
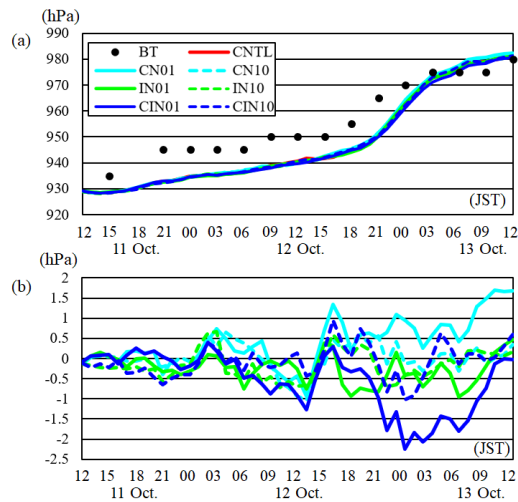
Figure 1. Time series of (a) RMSC Tokyo BT central pressure and simulated central pressures, and (b) differences of central pressure in the sensitivity experiments from that in CNTL.
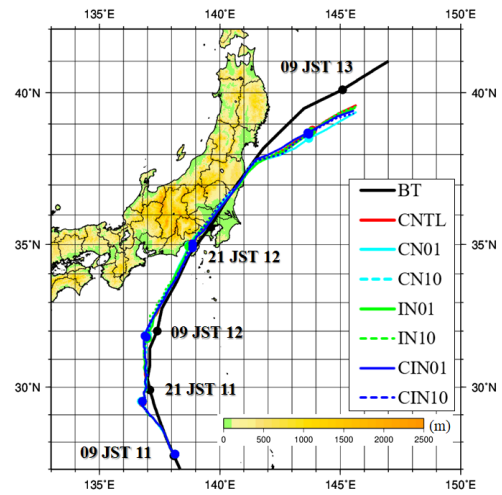
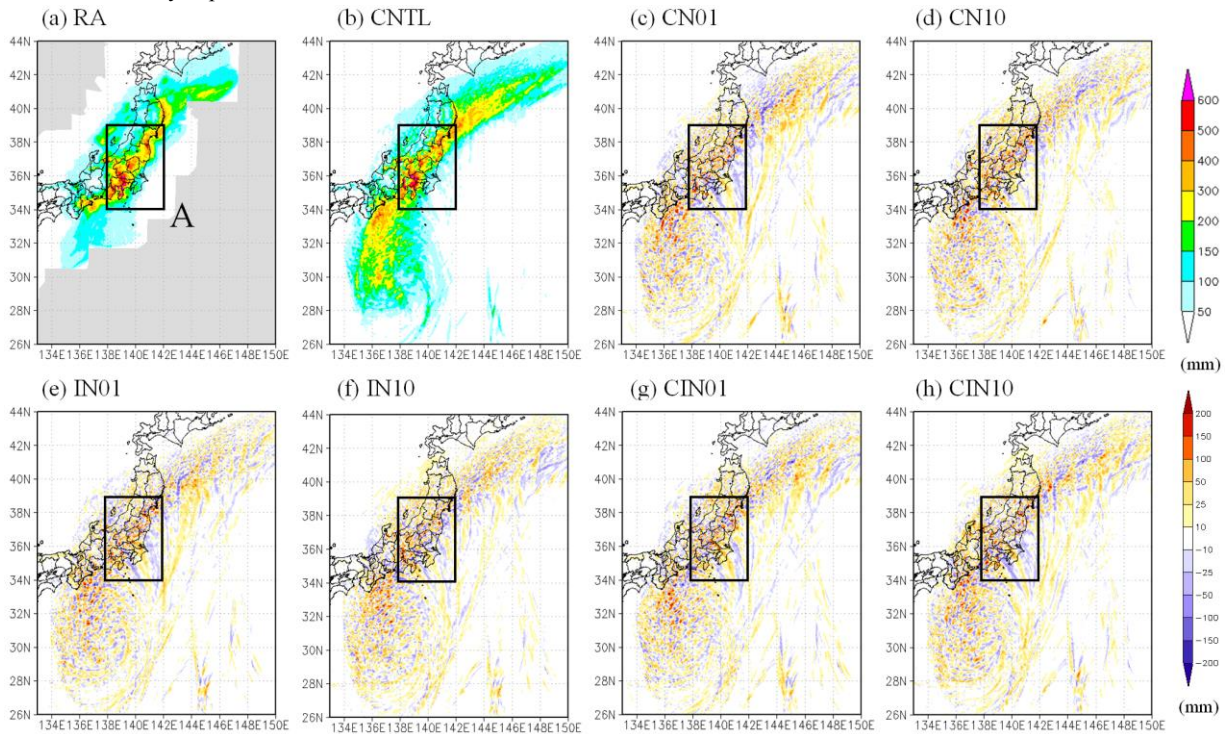Figure 2. RMSC Tokyo BT and simulated tracks from 09 JST on 11 October to 12 JST on 13 October.

Figure 3. Horizontal distribution of precipitation amounts from 09 JST on 11 to 12 JST on 13 October 2019 in (a) radar analysis (RA), (b) CNTL, and (c)-(h) the differences from CNTL for each experiment.

Table 1. Summary of central pressures at the longitude of 138.7˚E and precipitation amounts. The values under the precipitation amounts from 09 JST on 11 to 12 JST on 13 October of each sensitivity experiment indicate the changes (%) from the precipitation amount of CNTL.

	BT / RA	CNTL	CN01	CN10	IN01	IN10	CIN01	CIN10
Central pressure at longitude 138.7°E (hPa)	955	949.6	951.2	950.1	949.2	950.4	948.3	949.2
Averaged precipitation amount in all domain (mm)	-	29.6	29.8	29.6	29.6	29.8	29.8	29.8
			0.4 %	-0.1 %	0.0 %	0.4 %	0.4 %	0.4 %
Averaged precipitation amount in domain A (mm)	163.8	161.3	158.8	164.3	161.0	159.9	163.0	157.6
			-1.5 %	1.8 %	-0.1 %	-0.9 %	1.1 %	-2.3 %
Maximum precipitation amount in domain A (mm)	1346.1	788.5	705.6	735.4	876.6	797.7	700.4	709.7
			-10.5 %	-6.7 %	11.2 %	1.2 %	-11.2 %	-10.0 %

References:

Araki, K., 2020: Numerical simulation of heavy rainfall event associated with typhoon Hagibis (2019) with different horizontal resolutions. *Research Activities in Earth System Modelling*, *Working Group on Numerical Experimentation*, **50**, *WMO, Geneva*, p.3.03–3.04.

Improved representation of convective moistening
in JMA's next-generation coupled seasonal prediction system

KOMORI Takuya*, HIRAHARA Shoji and SEKIGUCHI Ryohei

Climate Prediction Division, Japan Meteorological Agency, Tokyo, Japan

Email: komori@met.kishou.go.jp

1. Introduction

The Japan Meteorological Agency (JMA) is developing the next-generation Coupled Seasonal Ensemble Prediction System version 3 (JMA/MRI-CPS3; CPS3), which consists of 60km atmospheric components and an eddy-permitting (0.25 deg.) ocean component. In addition to supporting three-month, warm-/cold-season and El Niño forecasts, CPS3 will provide sea surface temperature (SST) data as a lower boundary condition in JMA's Global Ensemble Prediction System (GEPS) for a two-tiered SST approach (Takakura and Komori, 2020). Since GEPS supports the issuance of operational typhoon information as well as one-week, two-week and one-month forecasts, CPS3 prediction skill in light of the link between operational weather and climate predictions is crucial. This report details results from verification of convective moistening in CPS3.

2. Revised convection scheme in CPS3

CPS3 involves the use of the prognostic Arakawa-Schubert convection scheme with a spectral cloud ensemble and prognostic closure with certain modifications (JMA 2019). The scheme is revised after Komori and Shimpo (2016) with modifications focusing on moistening processes in the tropics:

a) Introduction of relative humidity (RH)-dependent formulation inspired by Bechtold et al. (2008) for entrainment $\varepsilon(z,t,i)$ in updraft mass flux:

$$\varepsilon(z,t,i) = \varepsilon'(t,i)f\left(\overline{RH}(z)\right)$$

$$f\left(\overline{RH}(z)\right) = \left((RH_c - 1)\frac{\overline{q_s}(z)}{\overline{q}(z)} + \frac{\overline{q_s}(z) - \overline{q}(z)}{\overline{q}(z)}\right) \times \left(\frac{\overline{q_s}(z)}{\overline{q_s}(z_B)}\right)^\propto$$

$$= \left(\frac{RH_c - \overline{RH}(z)}{\overline{RH}(z)}\right) \times \left(\frac{\overline{q_s}(z)}{\overline{q_s}(z_B)}\right)^\propto$$

   Here, the constant parameter $RH_c = 1.1$, and $\varepsilon'(t,i)$ is diagnosed for each convective plume i at every time step t depending on the environmental profile of moist static energy. $\overline{q}$ and $\overline{q_s}$ are specific humidity and saturation specific humidity in the environment, respectively. z_B is the convective cloud bottom height, and $\propto$ is a constant.

b) Loosening of the upper limit of the entrainment rate for shallow convection with cloud top lower than 700 hPa.

3. Experimental configuration and results

The current configuration of CPS3 (TEST) was compared to the configuration without the revision of the convection scheme (CNTL) in three experiments with different forecast ranges and model resolutions. Verification of 72-hour forecasting against the RH of ERA5 reanalysis (Hersbach et al., 2020) and GPCC precipitation (using the atmospheric component of CPS3 with 120-km resolution) in July and August 2009 showed that the convection scheme revision significantly improved vertical RH profiles depending on precipitation over the Indian Ocean (Figure 1). As expected, the normalized number of precipitation occurrences was also improved as a result of better convective moistening due to the effect of RH-dependent entrainment.

In relation to medium-range forecasting, error growth for the specific humidity profile in the tropics was also verified against radiosonde observation during the 11-day forecast in an experiment on analysis (data assimilation) and forecast cycles in August 2018 using the atmospheric component of CPS3 with 20km resolution. The results demonstrated that TEST outperformed CNTL with less bias and smaller error growth (Figure 2).

As a verification of convectively coupled equatorial waves in long-range forecasts, wavenumber-frequency spectra with an equatorially symmetric component of the OLR (simulated over the period from 2001 to 2007 using the atmosphere-ocean coupled model with the same resolution as CPS3) showed TEST improved the too small amplitude and too high frequency of Kelvin wave in CNTL, as compared to NOAA AVHRR satellite observation (Figure 3). Overall, the revision of the convection scheme showed encouraging results with significant improvement of prediction for many aspects of moistening processes in tropics.

REFERENCE

Bechtold P., M. Kohler, T. Jung, F. Doblas-Reyes, M. Leutbecher, M. Rodwell, F. Vitart and G. Balsamo, 2008: Advances in simulating atmospheric variability with the ECMWF model: From synoptic to decadal timescales. *Q. J. R. Meteorol. Soc.*, **134**, 1337–1351.

Hersbach, H., B.Bell, P. Berrisford, S. Hirahara, András Horányi1, J. Muñoz-Sabater, J. Nicolas, C. Peubey, R. Radu, D. Schepers, A. Simmons, C. Soci, S. Abdalla, X. Abellan, G. Balsamo, P. Bechtold, G. Biavati, J. Bidlot, M. Bonavita, G. De Chiara1, P. Dahlgren, D. Dee, M.

Diamantakis, R. Dragani, J. Flemming, R. Forbes, M. Fuentes, A. Geer, L. Haimberger, S. Healy, R.J. Hogan1, E. Hólm, M. Janisková, S. Keeley, P. Laloyaux, P. Lopez, G. Radnoti, P. de Rosnay, I. Rozum, F. Vamborg, S. Villaume and J.-N. Thépaut, 2020: The ERA5 Global Reanalysis. *Q. J. R. Meteorol. Soc.*, accepted.

Komori, T. and A. Shimpo, 2016: Improvement of MJO prediction and moistening processes for the DYNAMO period. *CAS/JSC WGNE Research Activities in Atmospheric and Oceanic Modeling,* 4.05-4.06.

Takakura, T and T. Komori, 2020: Two-tiered sea surface temperature approach implemented to JMA's Global Ensemble Prediction System. *CAS/JSC WGNE Research Activities in Atmospheric and Oceanic Modeling*, submitted.

JMA, 2019: Outline of the operational numerical weather prediction at the Japan Meteorological Agency. Appendix to WMO technical progress report on the global data-processing and forecasting system and numerical weather prediction research. 188pp. Available online: http://www.jma.go.jp/jma-eng/jma-center/nwp/outline2019-nwp/index.htm
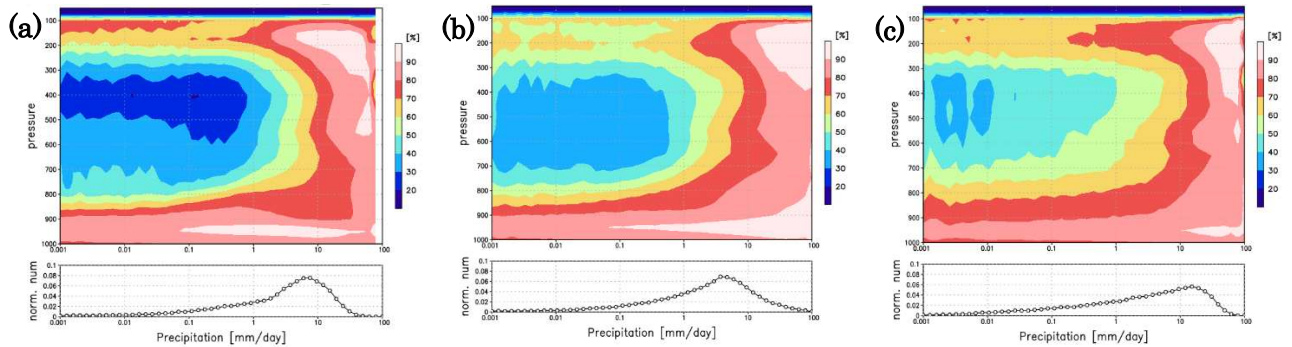
Figure 1. Vertical RH profiles [%] (shading) depending on precipitation [mm/day] averaged over 72-hour forecasts using the atmospheric component of CPS3 in July and August 2009 over the Indian Ocean for (a) CNTL and (b) TEST with reference to (c) ERA5 and GPCC. The normalized number of precipitation occurrences is shown in the bottom figure.
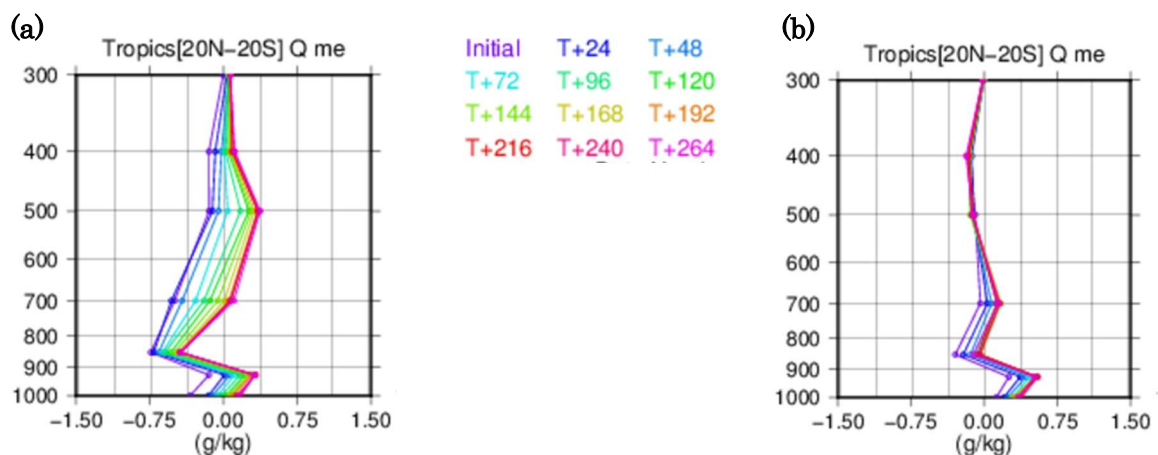

Figure 2. Forecast error growth for specific humidity [g/kg] averaged over the tropics (20°S – 20°N) in an analysis-and-forecast cycle experiment using the atmospheric component of CPS3 with 20km resolution: (a) CNTL and (b) TEST. Colored profiles show forecast errors against radiosonde observations at each forecast time averaged over August 2018.
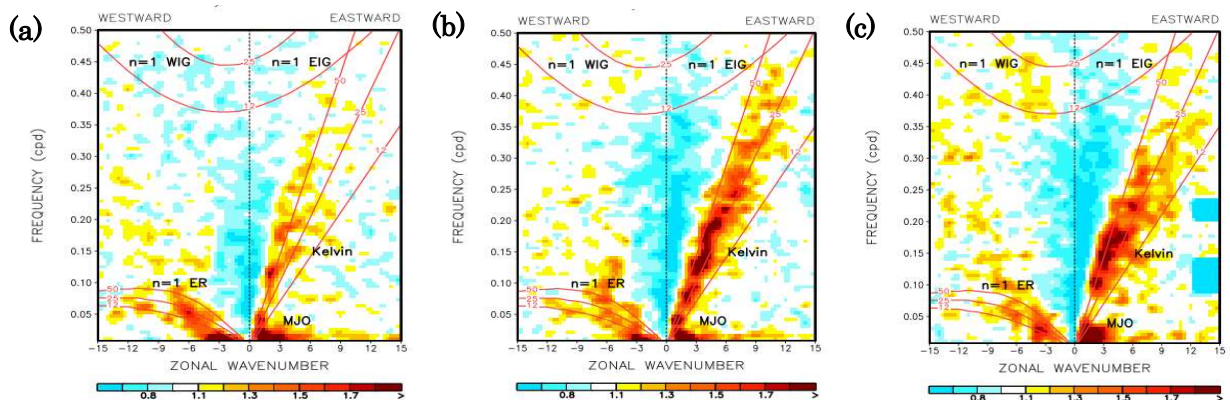

Figure 3. Wavenumber-frequency power spectra with an equatorially symmetric component of the OLR (15°N – 15°S) in experiments using the atmosphere-ocean coupled model with the same resolution as CPS3: (a) CNTL, (b) TEST and (c) NOAA AVHRR satellite observation from 2001 to 2007.

A new Estimated Inversion Strength (EIS) based on the moist-air entropy.
by Pascal Marquet[1] and Peter Bechtold[2]

[1]Météo-France. CNRM/GMAP. Toulouse. France. *E-mail: pascal.marquet@meteo.fr*
[2]European Centre for Medium-Range Weather Forecasts (ECMWF), Reading, UK Bologna, Italy.

1) Motivations - Introduction.

Distinguishing between cumulus and well-mixed stratocumulus is an important component of the IFS boundary-layer scheme (https://www.ecmwf.int/en/elibrary/18714-part-iv-physical-processes.

Klein and Hartmann (1993) showed empirically that the stratus cloud cover increases with the "Lower Tropospheric Stability" of the atmosphere defined as LTS = $\theta_{700hPa} - \theta_{surf}$ (namely the difference in dry potential temperature $\theta = T\,(p_0/p)^{0.2857}$ between the level 700 hPa and the surface, where $p = 1000$ hPa).
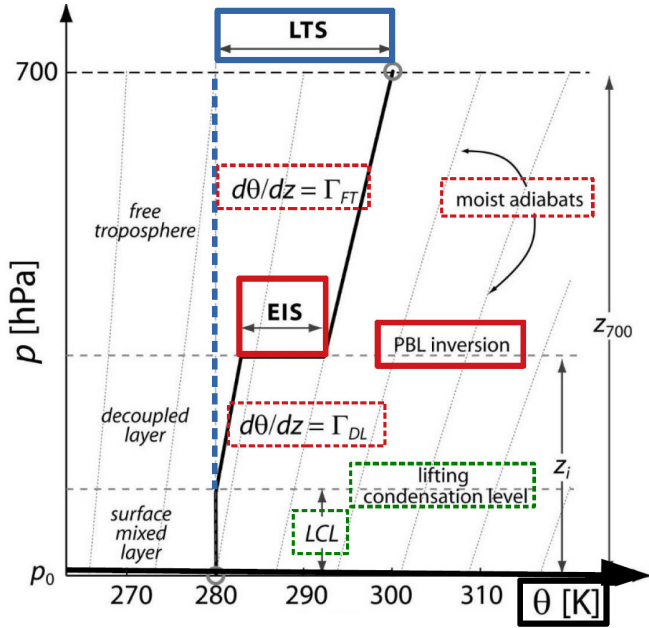

Figure 1: *The same Fig.1 of WB06 with coloured boxes.*

Wood and Bretherton (2006, WB06) defined a revised formulation of the inversion strength called the "Estimated Inversion Strength" (EIS) that is a better predictor for the stratus cloud cover than the LTS. If a cloud is detected in an unstable boundary layer, a threshold value of about 7 K is adopted for distinguishing whether it is a stratocumulus (EIS > 7) or a shallow cumulus (EIS < 7).

The definition EIS = LTS $- \Gamma_m^{850}\,(z_{700} - \text{LCL})$ depends both on the mean vertical lapse rate Γ_m^{850} (computed at 850 hPa) and the difference in the height of the 700 hPa and Lifting Condensation levels. It is clearly shown in Fig. 1 that EIS<LTS.

Figs. 2 shows the large impact of the thresholds EIS > 8 or EIS > 10 in the IFS on the mean model bias of the net shortwave radiation at the top of the
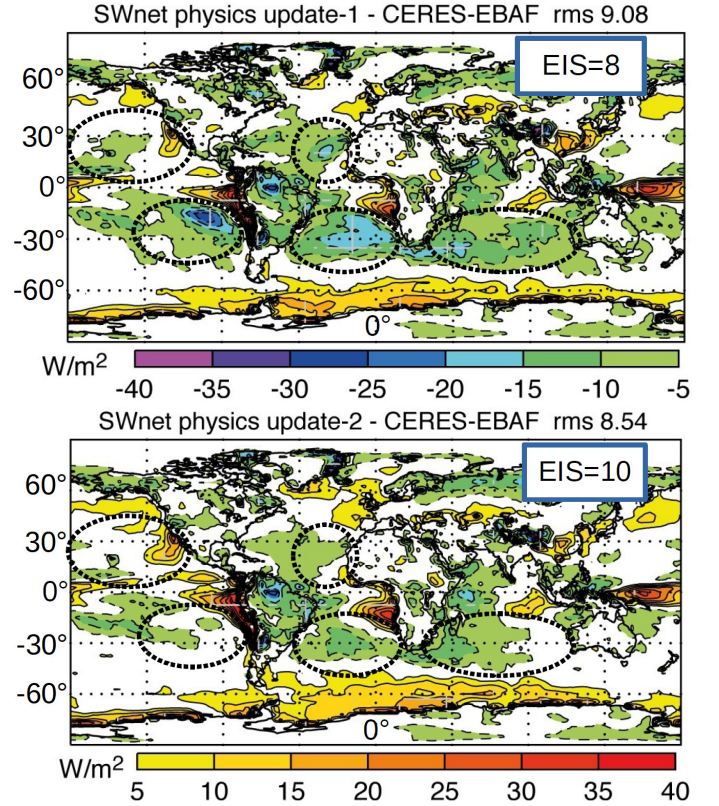

Figure 2: *The impact of the threshold for EIS on the bias of net short-wave for IFS forecasts compared to the CERES-EBAF climatology. Thresholds: EIS > 8 (top) and EIS > 10 (bottom)*

atmosphere compared to observations by changing the low cloud cover and the optical thickness.

However, the definition of EIS is complex (it depends on the saturation conditions via Γ_m^{850}) and non-linear (product of "Γ_m^{850}" with "$z_{700} - \text{LCL}$") and is likely not suitable for more stable boundary-layer conditions over land. Therefore we evaluated the application of the moist-air entropy variable defined in Marquet (2011, M11).

2) Use of the moist-air entropy MSE.

The specific absolute moist-air entropy (s) is defined in M11 in terms of an entropy potential temperature θ_s so that $s = s_0 + c_{pd}\,\ln(\theta_s)$, where $s_0 \approx 1139$ kJ/K/kg and $c_{pd} \approx 1004.7$ kJ/kg are two constant terms. In order to get a quantity more linear than θ_s, it is possible to use as a proxi the "moist entropy static energy" S_m defined by Eq.73 of M11, but generalized to the ice-liquid conditions, to give

$$S_m = c_{pd}\,(1 + 5.87\,q_t)\,T - L_v\,q_l - L_s\,q_i + g\,z, \quad (1)$$

where z is the height (in m), $g \approx 9.80665$ m/s² the acceleration of gravity, L_v and L_s the latent heats of

vaporization and sublimation, and $q_t = q_v + q_l + q_i$, q_v, q_l and q_i are the total water, water vapour, liquid water and ice specific contents, respectively. The new large coefficient 5.87 is the key parameter that allow θ_s or S_m to represent the absolute entropy.
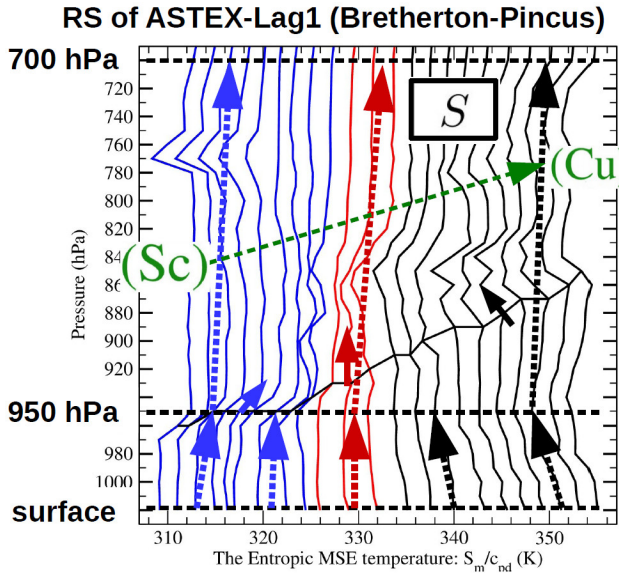

Figure 3: *Plots of vertical profiles of $S = S_m/c_{pd}$ (K) for the first ASTEX Lagrangian experiment (see the main text).*

Vertical soundings of the first ASTEX Lagrangian experiment (Bretherton and Pincus, 1995, de Roode and Duynkerke, 1997) have been used in Fig. 3 to compute the profiles of $S = S_m/c_{pd}$ for stratocumulus boundary-layers (left, in blue) and for cumulus boundary-layers (right, in black). The red profiles correspond to the transition between the regimes. (see: `http://www.atmos.washington.edu/~breth/astex/lagr/README.hourly.html`)

An interesting feature depicted by the solid arrows (and the dashed ones between the surface to the level 950 hPa) is that the transition from stratocumulus toward cumulus regimes occurs for constant values of S_m in the vertical from the surface to about 850 hPa, including across the top-PBL entrainment region. These results were already shown in M11, where a CTEI criterion was built with the simple hypothesis $\partial \theta_s/\partial z \approx 0$ corresponding to $\partial S_m/\partial z \approx 0$ at the top of the PBL.

A new EIS index is then defined as follow:

$$\text{EIS}_{\text{new}} = \text{Max}\left(S_{700} - S_{950} \, ; \, S_{950} - S_{\text{surf}}\right) . \quad (2)$$

The respective two moist entropy differences intend to reflect: i) the typical boundary-layer structures over water, with cloud base typically around 950 hPa; and ii) also more shallow boundary-layers over land in higher latitudes or during transitions.

Figs. 4 show the old (top) and new (bottom) EIS index computed for a run of the operational IFS model. The present criteria EIS > 8 for delimiting strong stable stratocumulus is replaced by the new one EIS$_{\text{new}} > 6$, with cumulus regimes delimited by
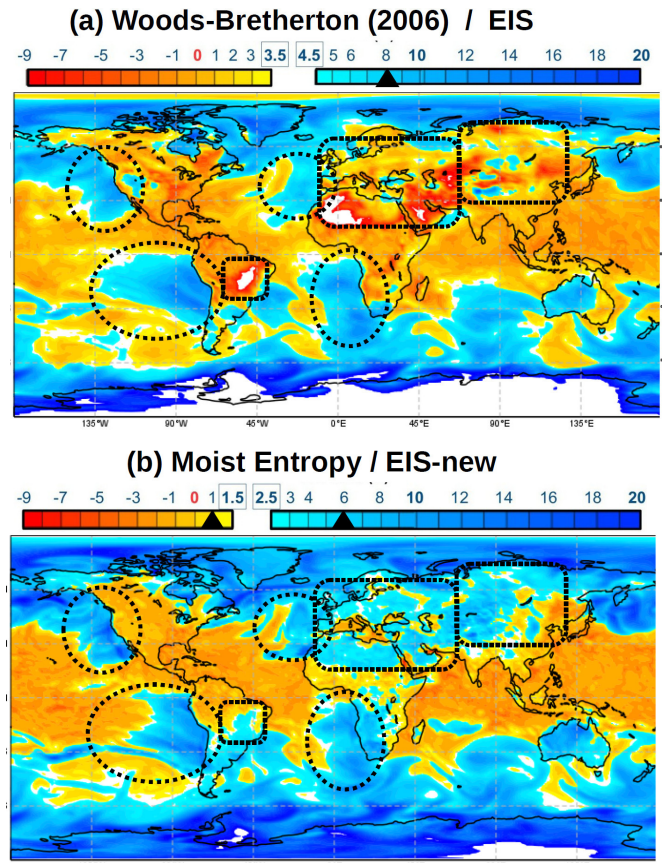

Figure 4: *Old (top) and new (bottom) EIS computed with IFS.*

EIS$_{\text{new}} < 1$. The new formulation more clearly delimits the boundary-layer transitions in the subtropical anticyclones, exhibits finer and more marked filaments and shows a clear distinction between nighttime and daytime boundary-layer stability over land..

3) Conclusions.

It is shown in this note that it is possible to use the proxi $S = S_m/c_{pd}$ of the moist-air entropy $s(\theta_s)$ to build a new EIS index based on the hypothesis of a transition between stratocumulus and cumulus regimes occurring for zero (or small) vertical changes of S, S_m and $s(\theta_s)$.

The new EIS index is simpler and more linear than the one derived in WS08 and is planned for introduction in IFS cycle 48r1 (2020) in the context of a larger moist physics upgrade.

References

● Bretherton, C. S. and Pincus, R. (1995). Cloudiness and marine boundary layer dynamics in the ASTEX lagrangian experiments. Part I: Synoptic setting and vertical structure. *J. Atmos. Sci.*, **52**: 2707–2723.

● Klein, S. A. and Hartmann, D. L. (1993). The seasonal cycle of low stratiform cloud. *J. Climate*, **6**: 1587–1606.

● Marquet P. (2011). Definition of a moist entropic potential temperature. Application to FIRE-I data flights. *Q. J. R. Meteorol. Soc.*, **137**: 768–791. `https://arxiv.org/abs/1401.1097`

● Wood R, Bretherton C. S. (2006). On the relationship between stratiform low cloud cover and Lower-tropospheric stability. *J. Climate*, **19**: 6425–6432.

Evaluation of revised gravity wave parametrizations using statistics of first-guess departures

MATSUKAWA Chihiro, YONEHARA Hitoshi and KANEHAMA Takafumi

Japan Meteorological Agency, Tokyo, Japan

Email: chi_matsukawa@met.kishou.go.jp

1. Introduction

The effects of unresolved gravity waves, which significantly affect the accuracy of numerical weather prediction (NWP), are parametrized individually in subgrid-scale orography (SSO) parametrization and non-orographic gravity wave (NGW) parametrization in global models. Although such parametrization exhibits considerable uncertainty due to a lack of direct observation for momentum flux, it can be evaluated indirectly using the massive volume of various kinds of observation which is available through data assimilation in the NWP system. In this study, the performance of the revised NGW and new SSO parametrizations in the Japan Meteorological Agency Global Spectral Model (JMA GSM; JMA 2019) was individually examined in terms of statistics of fitting between first-guess (FG) and observation (i.e., FG departure (observation minus first guess in 3 – 9 h forecasts)) processed in data assimilation.

2. Non-orographic Gravity Waves (NGW)

The latitude-dependent function that reduces launch flux near the equator is incorporated into the source momentum flux in the NGW scheme (Scinocca 2003; ECMWF 2014). In addition, the vertical diffusion coefficient in the turbulent diffusion scheme is damped with the cubic function of pressure above the diagnosed tropopause in stable conditions.

This improves the representation of quasi-biennial oscillation in long integration over that of previous parametrization with uniform source momentum flux (not shown). The revised scheme also significantly reduces the standard deviations of FG departures in the tropical stratosphere, especially for microwave

sounders and radiosondes as shown in Fig. 1, additionally providing positive impacts on short-range forecasts in data assimilation.

3. Subgrid-scale Orography (SSO)

A new set of parametrizations representing subgrid-scale orographic drag, including the effects of low-level flow blocking and orographic gravity wave drag (OGWD) as proposed by Lott and Miller (1997) and the turbulent orographic form drag proposed by Beljaars et al. (2004), is implemented. The performance of this set of parametrizations is compared with the OGWD scheme presented by Iwasaki et al. (1989), which was used in the GSM and incorporates two types of gravity wave drag affecting areas from the upper troposphere to the lower troposphere, and from the surface to the lower troposphere.

The revised SSO parametrization mitigates positive geopotential height biases around the East Asia in the Northern Hemisphere winter troposphere and improves medium-range forecasts skill. These impacts are also seen in the standard deviations of FG departures for the radiosonde zonal wind velocity shown in Fig. 2. However, this parametrization is also seen to cause a deterioration in FG departures for microwave sounding channels and radiosondes in the stratosphere over areas of steep orography (e.g., the Himalayas, the Southern Andes and the Antarctic Peninsula) in the winter hemisphere. This suggests that further improvement of gravity wave momentum flux generation and vertical profiles of orographic gravity wave breaking is required, particularly in regions with larger FG departure values.

References

Beljaars, A., A. R. Brown, and N. Wood., 2004: A new parametrization of turbulent orographic form drag. *Q. J. R. Meteorol. Soc.*, **130**, 1327-1347.

ECMWF, 2014: Part IV Physical Processes, Chapter 5 Non-orographic gravity wave drag. *IFS documentation – Cy40r1*, 67-72.

Iwasaki, T., S. Yamada, and K. Tada, 1989: A Parameterization Scheme of Orographic Gravity Wave Drag with Two Different Vertical Partitionings Part I: Impacts on Medium-Range

Forecasts. *J. Meteor. Soc. Japan*, **67**, 11-27.

Japan Meteorological Agency 2019: *Outline of the operational numerical weather prediction at the Japan Meteorological Agency.* JMA.

Lott, F. and M. J. Miller, 1997: A new subgrid-scale orographic drag parametrization: Its formulation and testing. *Q. J. R. Meteorol. Soc.*, **123**, 101-127.

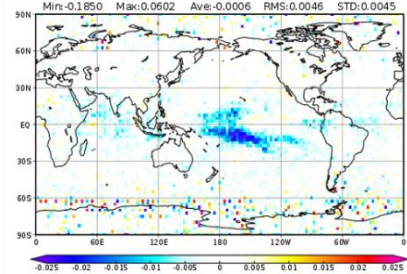Scinocca, J. F. 2003: An Accurate Spectral Nonorographic Gravity Wave Drag Parameterization for General Circulation Models. *J. Atmos. Sci.*, **60**, 667-682.
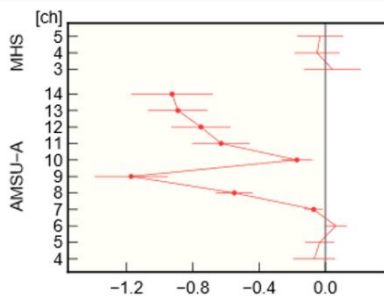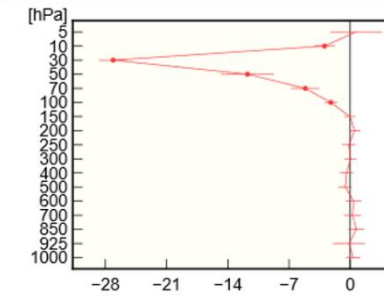
Fig. 1 Normalized changes [%] in the standard deviation of FG departures in the tropics (20°N – 20°S) for (a) microwave temperature sounders and humidity sounders (AMSU-A, MHS), and (b) radiosonde zonal wind velocity. (c) Spatial distribution of changes in root mean square FG departures for AMSU-A/Ch. 9 brightness temperature [K]. The period is from Jul. 21 to Sep. 11 2017. Negative values show RMSE reductions with the revised scheme. Error bars and dots in (a, b) indicate 95% confidence intervals and statistically significant changes, respectively.
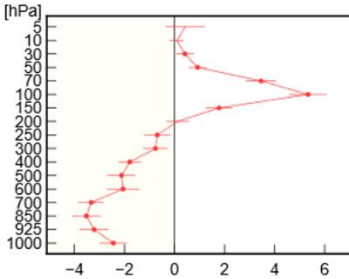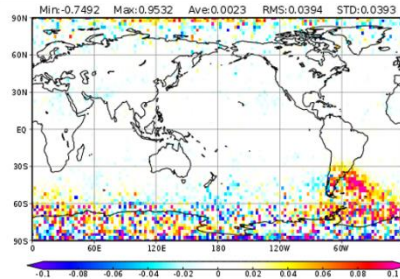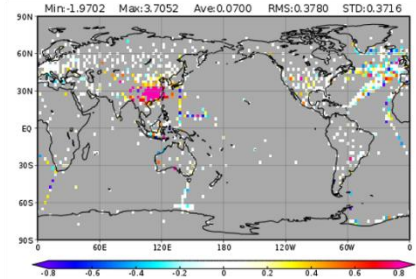

Fig. 2 (a) Same as in Fig. 1 (b), but for the Northern Hemisphere (20°N – 90°N) from Dec. 21 2017 to Feb. 11 2018. (b, c) Same as in Fig. 1 (c), but for (b) AMSU-A/Ch. 14 brightness temperature [K] from Jul. 21 to Sep. 11 2017. (c) Radiosonde zonal wind velocity [m/s] at 100 hPa from Dec. 21 2017 to Feb. 11 2018.

Relationship between intensity and duration of tropical cyclones

I.I. Mokhov[1,2], A.G. Poroshenko[2]

[1]A.M. Obukhov Institute of Atmospheric Physics RAS, Moscow, Russia

[2]Lomonosov Moscow State University, Moscow, Russia

mokhov@ifaran.ru

Using long-term data for tropical cyclones (TC), estimates of the relationship of their characteristics are made in comparison with model considerations based on the simplest parameterizations. In particular, quantitative estimates of the relationship between the TC intensity and duration in the North-West Pacific Ocean (NWPO) with the use of the RSMC data (http://www.jma.go.jp/jma/jma-eng/jma-center/rsmc-hp-pub-eg/) for the past decades are presented.

Figure 1 shows the dependence of the TC lifetime τ on their maximum intensity I (maximum Δp) in the NWPO from the RSMC data for the period 1951-2019. The TC intensity I is characterized by a pressure drop Δp at sea level between the background and the TC center similar to [1]. The TC lifetime τ is determined in days.
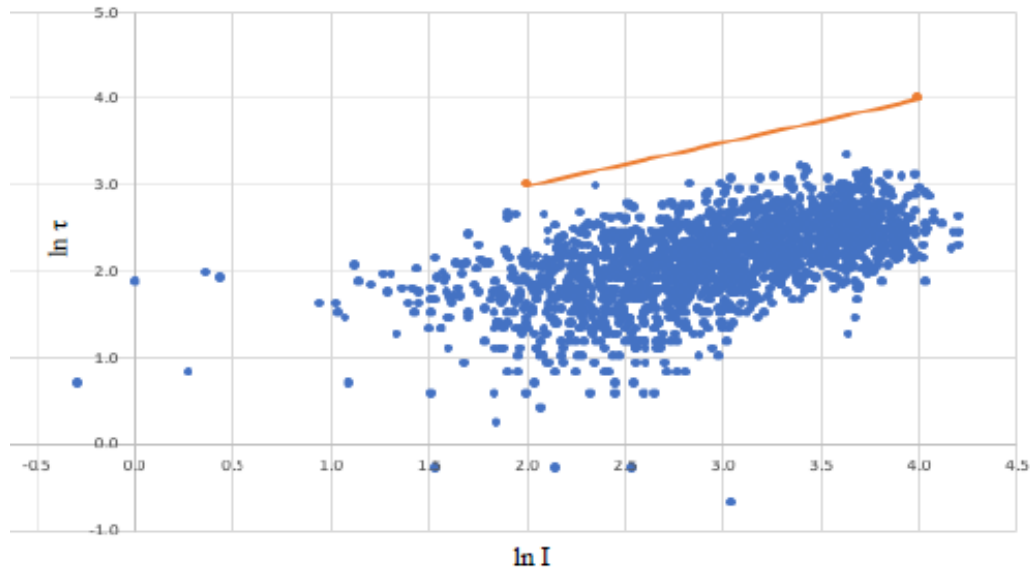

Figure 1. The dependence of the TC lifetime τ on their intensity I in the NWPO from the RSMC data for the period 1951-2019.

According to Fig. 1, the relationship between $ln\ \tau$ and $ln\ I$ for 1812 analyzed TCs can be approximated by a linear dependence

$$ln\ \tau \sim k\ ln\ I \qquad (1)$$

with $k = 0.45$ with a correlation coefficient for the corresponding linear regression $r = 0.58$. The linear dependence (1) corresponds to a power-law dependence of τ on I (Δp):

$$\tau \sim I^k . \qquad (1a)$$

A similar analysis was made for the relationship between the time (τ_i) of TC reaching its maximum intensity I (Δp), as well as between the lifetime and maximum intensity of TC that reached extratropical latitudes. In particular, for the corresponding linear regression of $\ln \tau_i$ on $\ln I$, according to the data for 1812 analyzed TCs in the NWPO, an exponent $k_i = 0.43$ was obtained with a correlation coefficient $r = 0.43$.

The results obtained are close to the estimates presented in [3] for shorter data series for the 20-year period 1970-1989 according to GTECCA. In [3] (see also [2]), the following estimates were obtained: $k = 0.50$, $k_i = 0.44$. The statistical results obtained can be explained using a simple model for the development of TC based on the energy balance for the kinetic energy E_K with the simplest parameterizations.

The E_K value increases due to the heat flux from the ocean (F_H):

$$\partial E_K/\partial t \sim F_H,$$

where $E_K \sim V^2$ with a characteristic wind speed V estimated by the tangential wind speed. The value of V^2 for the TC is proportional to the pressure Δp (I) between the center and the periphery of the TC: $\Delta p \sim V^2$. The heat flux F_H can be parameterized as

$$F_H \sim C_H V,$$

where C_H is the heat transfer coefficient, respectively. From (1) it follows

$$\partial V^2 / \partial t \sim V.$$

and the TC characteristic time τ is proportional to V or

$$\tau \sim (\Delta p)^{1/2}. \qquad\qquad (2)$$

Figure 1 shows corresponding to dependence (2) straight line with slope in a good agreement with the general dependence of the lifetime on the intensity of TCs in the NWPO, estimated from the RSMC for the last 7 decades.

References

1. Golitsyn G.S., Demchenko P.F., Mokhov I.I., Priputnev S.G. (1999) Tropical cyclones: statistical regularities of distribution functions depending on intensity and lifetime. *Doklady Earth Sci.*, **366** (4), 537–542.
2. Intense Atmospheric Vortices and their Dynamics. Ed. by I.I. Mokhov, M.V. Kurgansky, O.G. Chkhetiani. Moscow, GEOS, 2018, 482 p. (in Russian)
3. Mokhov I.I., Priputnev S.G. (1999) Tropical cyclones: Statistical and model relations between intensity and duration. Research Activities in Atmospheric and Oceanic Modeling. Ed. By H. Ritchie. WMO/TD-No.942, 2.22-2.23.

Testing a New Horizontal Mixing-length Formulation in HMON

Weiguo Wang[1], Lin Zhu[1], Hyun-Sook Kim[1], Dan Iredell[1], Keqin Wu[1], Bin Liu[1], Zhan Zhang[1],
Avichal Mehra[2], Vijay Tallapragada[2]
[1]IMSG @ EMC/NCEP/NWS/NOAA, [2]EMC/NCEP/NWS/NOAA, College Park, MD 20740
Email: Weiguo.Wang@noaa.gov

1. Introduction

Recent studies indicate that the intensity of numerically-simulated tropical cyclones (TC) are sensitive to the horizontal mixing length (L_h) in the parameterization of horizontal diffusion. A fixed fraction of the model grid spacing or a constant value is usually used to approximate L_h in many current numerical models. This approximation is not in agreement with L_h derived from observational data and large eddy simulations. To improve the representation of horizontal diffusion in numerical models, we proposed a new formulation of L_h, which is a function of horizontal wind and its gradients. The new formulation has been used in HWRF to simulate Hurricane Harvey (2017) and showed very positive impacts (Wang et al, 2020). In one of the experiments supporting the upgrade of HMON model in 2020, we tested the new formulation in the latest HMON system. A brief description of the experiment and results are shown.

2. New formulation

Details of the new formulation are given in Wang et al. (2020). Here only a basic idea of the new formulation is given. The horizontal exchange coefficient K_h is calculated as, $K_h = L_h^2 |D_h|$ where D_h is proportional to horizontal deformation. In many current numerical models, L_h is given as
$$L_h = Constant\ or\ \alpha\Delta,$$
where α is a constant, Δ is model horizontal grid spacing. The new formulation is flow-dependent,
$$L_h = 0.5(L_{h1} + L_{h2}),$$
where L_{h1} and L_{h2} are the length scales for shear and stretching, respectively.

3. HMON (Hurricanes in a Multi-scale Ocean-coupled Non-hydrostatic) model in 2020

The operational deterministic HMON system contains two major components. The atmospheric component uses the Non-hydrostatic Multi-scale model on a B grid (NMMB) as its dynamic core. It is configured as triple-nested regional domains, with one parent domain and two movable nests. The ocean is simulated by HYCOM, coupled to NMMB through a coupler developed at NCEP. Large scale data are provided by the operational Global Forecast System (GFS) and Real-Time Ocean Forecast System (RTOFS). HMON is initialized every six hours, with a vortex relocation procedure. Compared with the 2019 version, major upgrades of the latest HMON system include: (1) the number of vertical levels increasing from 51 to 71; (2) using the original IGBP roughness length; (3) using the latest version of HYCOM, with a new version of mixed layer scheme, a C_d formula based on CORE v3, Newtonian relaxation employed in an implicit time step, and a corrected momentum reduction; (4) turning on the GWD option over the parent domain.

4. Results and discussion

As a control experiment (CNTL), the latest HMON 2020 was run to simulate 7 EPAC TCs in 2019, including Barbara 02E, Erick 06E, Flossie 07E, Juliette 11E, Kiko 13E, Mario 14E, and Lorena 15E. A fixed fraction of grid spacing is used in the CNTL as the horizontal mixing length over a given domain. They are 0.2, 0.2, and 0.3 for the parent and two nest domains, respectively. In the test run (EXPL), the new flow-dependent mixing length formulation is used in all domains. Figure 1 shows the track and intensity errors as well as mean bias for all verifiable cycles. Overall, the new formulation can improve the track forecast at almost all lead times. The intensity is improved before the 72nd hour but degraded by 4% after that. The EXPL produced TCs generally stronger than the CNTL did. Figures 2 and 3 show the verification plots for the runs (cycles) with intensity at initial time greater and less than 50 kt, respectively. For strong cycles, the new formulation improved both track and intensity slightly, but

increased the positive bias. For weak cycles, the new formulation improved the track by as much as 12%, but it degraded the intensity by as much as 20%. The positive mean bias is slightly increased.

In summary, preliminary test results for EPAC TCs suggest that the new formulation in general produced larger positive mean biases in intensity. In terms of RMS errors, it can help improve tracks for weak cycles and give positive impacts on both track and intensity for strong cycles. For individual TCs, the improvement in track for Eric 06E is the largest, with slightly better intensity. Juliette (11E) has the largest intensity improvement. Flossie (07E) has the most degradation in intensity, with a moderately degraded track. Investigations of individual runs are warranted to further understand the impact of the new formulation.
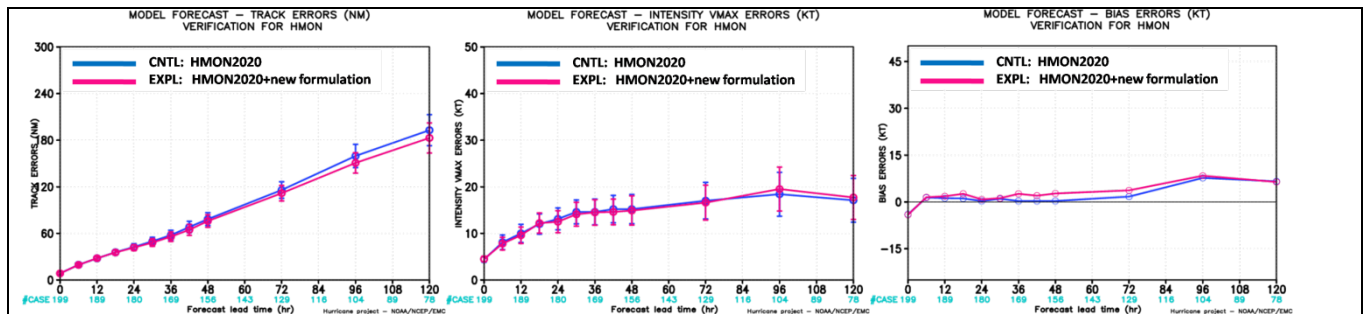

FIG. 1 Track errors (left). intensity errors (middle), and mean bias (right) of all verifiable cycles in two runs
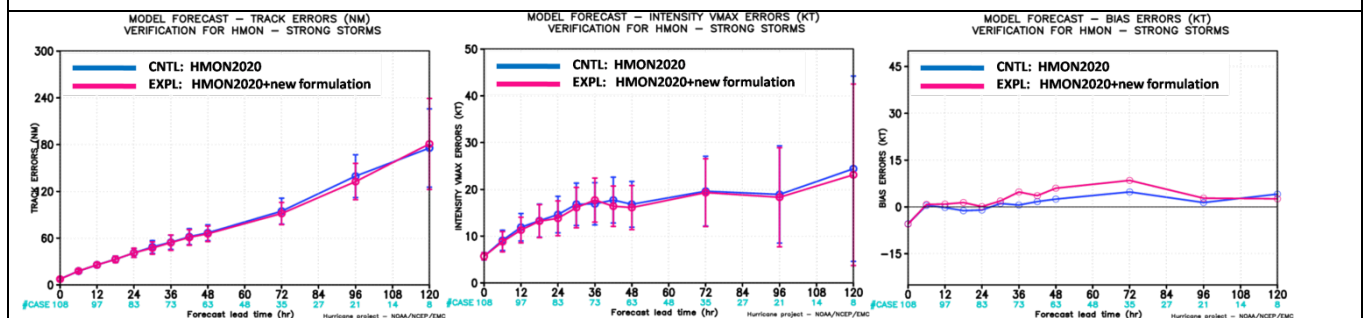

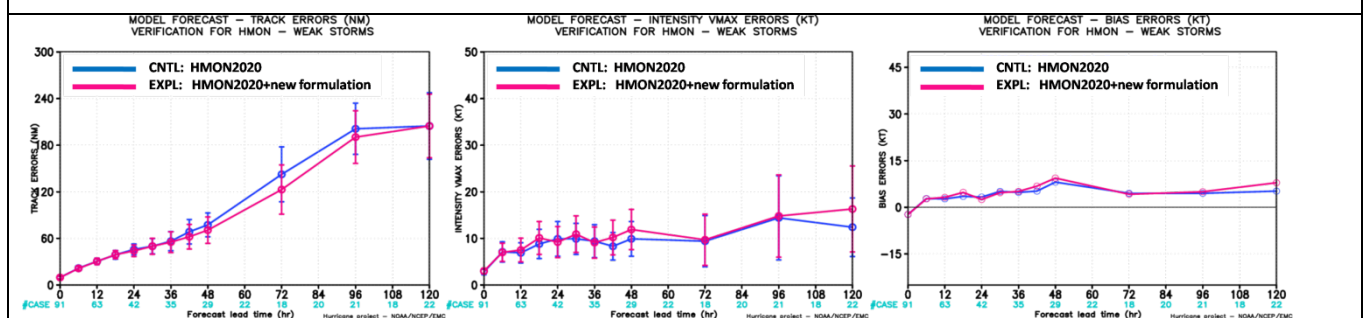FIG 2. As FIG 1 except for cycles of initial intensity greater than 50kt.

FIG 3. As FIG 1 except for cycles of initial intensity smaller than 50kt.

Reference:
(1) Weiguo Wang, Bin Liu, Lin Zhu, Zhan Zhang, Avichal Mehra, Vijay Tallapragada, 2020, A new horizontal mixing-length formulation for the simulations of tropical cyclones, to be submitted to **MWR**
(2) Weiguo Wang, Bin Liu, Lin Zhu, Zhan Zhang, Avichal Mehra, Vijay Tallapragada, 2020, A flow-dependent horizontal mixing length scale and its impact on track simulations of Harvey (2017) in HWRF. AMS 2020 annual meeting. Boston, MA, Jan, 2020
(https://ams.confex.com/data/handoutams/2020Annual/ Paper_364510_handout_5057_0.pdf)

Analysis and Mitigation of Occasional Precipitation-Type Problems in NCEP Global Forecast System

Weizhong Zheng[1], Jongil Han[2], Jack Kain[3], Geoffrey Manikin[3], Ruiyu Sun[1], Fanglin Yang[3] and Vijay Tallapragada[3]

[1]IMSG at NOAA/NCEP/EMC, College Park, MD 20740, USA; [2]SRG at NOAA/NCEP/EMC, College Park, MD20740, USA; [3]NOAA/NCEP/EMC, College Park, MD 20740, USA;
Email: Weizhong.Zheng@noaa.gov

1. Introduction

Recent diagnostic analyses by the National Centers for Environmental Prediction (NCEP) Model Evaluation Group (MEG), revealed that the NOAA Global Forecast System (GFS.v15) operational forecasts occasionally presented significant spurious warming in the lower troposphere during cold-season precipitation events. This behavior was detected in several events in the U.S. Midwest and Great Plains, where model-predicted warming led to inaccurate predictions of precipitation type, particularly a significant under-prediction of the areas where precipitation fell as snow. This study summarizes a diagnosis of the mechanisms for the spurious warming through a series of experiments involving the planetary-boundary-layer (PBL) and microphysics (MP) parameterization schemes.

2. Methodology

GFS.v15 has 64 vertical levels and applies the GFDL MP scheme and the hybrid eddy-diffusivity mass-flux (K-EDMF) PBL scheme that includes dissipative heating and modified stable boundary layer mixing (Han et al. 2016). In the series of experiments presented here, alternative parameterizations are used, including the Zhao-Carr and WSM6 MP schemes, along with the TKE-EDMF PBL scheme, which is a 1.5-order closure scheme predicting second-order turbulent kinetic energy of EDMF (Han and Bretherton, 2019) and is slated for implementation in GFS.v16 in early 2021. In addition to the different PBL and MP schemes, sensitivities to both the GFS.v15 and the 127-level GFS.v16 configuration are tested.

3. Forecast experiments

A representative erroneous warming event was evident in the operational GFS.v15 forecast initialized 00 UTC, 22 Jan, 2020. By the 36h forecast time, the GFS.v15 with the operational GFDL MP scheme predicted a temperature profile much warmer than observations between about 800 and 950 hPa and much colder between 600-800 hPa (Fig. 1). When either the Zhao-Carr or WSM6 MP scheme was substituted for the GFDL scheme, similar warm-cold anomalies did not develop (Fig. 1). Similar behavior occurs in the GFS.v16, in spite of its higher vertical resolution, when the same combination of K-EDMF PBL and GFDL MP schemes are used (Fig.2). However, substantial improvement is evident with the TKE-EDMF PBL scheme, regardless of the MP scheme used (Fig.3)

Additional diagnostics, including model temperature tendencies, revealed that the K-EDMF PBL scheme introduced strong vertical mixing across the observed stable layer between about 775 and 850 hPa. Specifically, the PBL scheme diagnosed a high amplitude, stratus-top-driven K profile in and near this layer, leading to strong vertical mixing, with warming below and cooling above the original stable layer. When this mixing mechanism was intentionally scaled back in the K-EDMF PBL scheme, the problem was essentially eliminated (Fig. 4). It remains unclear why, of the three MP schemes tested, only the GFDL MP scheme combines in a certain way with the K-EDMF scheme to trigger this behavior.

4. Summary

A series of sensitivity experiments with GFS.v15 and GFS.v16 were conducted to understand an occasional problem with prediction of precipitation-type in operational GFS.v15 forecasts. It was found that anomalous lower-tropospheric warming was responsible for the erroneous precipitation-type diagnosis and the warming was caused by a combination of the K-EDMF PBL and GFDL MP schemes. It was determined that the overly vigorous mixing can be essentially eliminated by modifying one component of the K-EDMF scheme's K-mixing profile. Nevertheless, additional study needs to be conducted to understand what specific environmental conditions and model-physics interactions lead to this undesirable model behavior.

References

Han, J., M. L. Witek, J. Teixeira, R. Sun, H.-L. Pan, J. K. Fletcher, and C. S. Bretherton, 2016: Implementation in the NCEP GFS of a hybrid eddy-diffusivity mass-flux (EDMF) boundary layer parameterization with dissipative heating and modified stable boundary layer mixing. Wea. Forecasting, 31, 341–352, doi:10.1175/WAF-D-15-0053.1.

Q. Zhao and F.H. Carr., 1997: A prognostic cloud scheme for operational nwp models. *Monthly Weather Review*, 125:1931–1953.https://doi.org/10.1175/1520 0493(1997)125<1931:APCSFO>2.0.CO;2

Hong, S.-Y., and J.-O. J. Lim, 2006: The WRF single-moment6-class microphysics scheme (WSM6).J. Korean Meteor. Soc.,42,129–151.

Han, J. and C. Bretherton, 2019: Scale-aware TKE-based moist eddy-diffusivity mass-flux (EDMF) parameterization for vertical turbulent mixing interacting with cumulus convection. Weather and Forecasting, 34, 869-886. https://doi.org/10.1175/WAF-D-18-0146.1
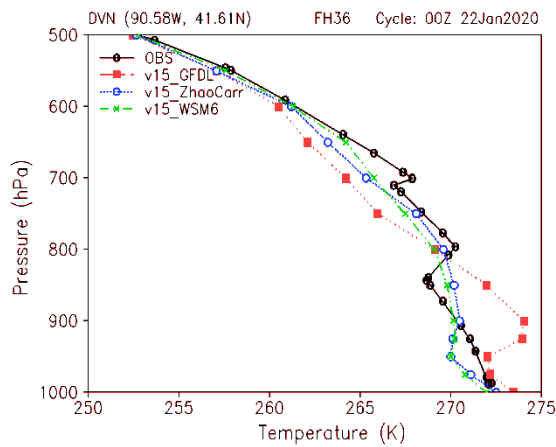
Fig.1. Atmospheric temperature profiles (K) against the sounding observations (black) at Davenport, IL, at 36-h forecast initiated at 00 UTC, 22 Jan, 2020. Three microphysics schemes utilized in GFS.v15 include GFDL (red), Zhao_Carr (blue) and WSM6 (green).
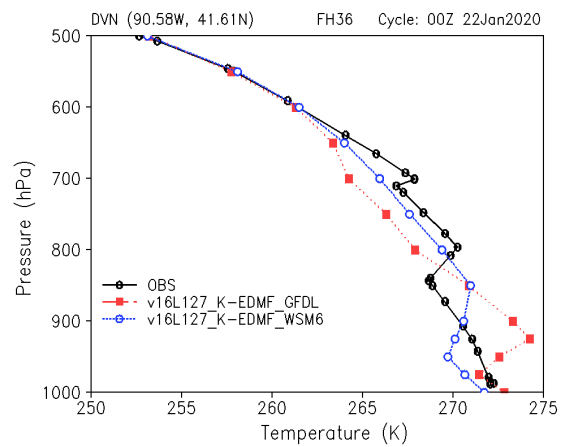

Fig. 2. The same as Fig.1, but for GFDL (red) and WSM6 microphysics schemes (blue) used in GFS.v16.
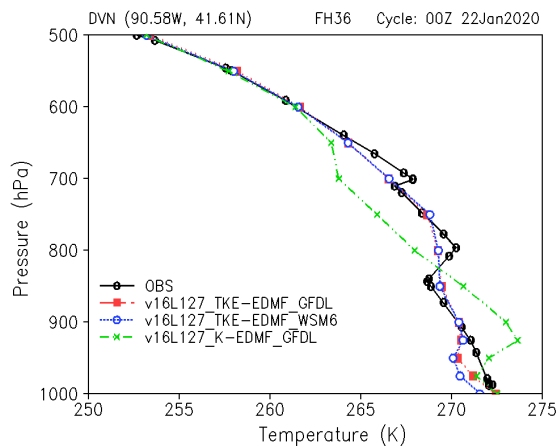

Fig. 3. The same as Fig.1, but for combination of TKE-EDMF PBL scheme with GFDL (red) or WSM6 (blue) microphysics schemes used in GFS.v16, compared to configuration of K-EDMF PBL scheme with GFDL microphysics scheme (green).
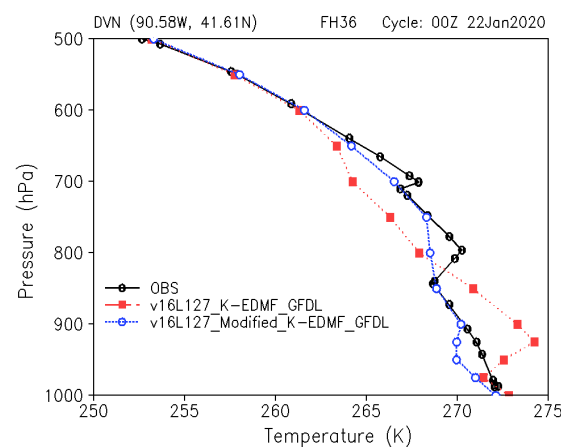

Fig. 4. The same as Fig.1, but for comparison between modified K-EDMF PBL scheme (red) and original K-EDMF PBL scheme (blue) combined with GFDL microphysics schemes used in GFS.v16.

Kurnell Storm (2015) simulations with high resolution UM

Hongyan Zhu*, Alain Protat and Charmaine Franklin, Research, Bureau of Meteorology, Australia

Email: *hongyan.zhu@bom.gov.au

1. Introduction

On 15th December 2015, the intense storm cell that originated around 35S on the coast, to the north of Sydney, approached Kurnell. This storm, now known as the Kurnell storm, induced local severe wind damage and flooding. The storm moved along the coastline northwards, undergoing further intensification and reached its maximum rainfall and rotating wind intensity around 23:30 UTC when it was passing Kurnell (Fig.1).
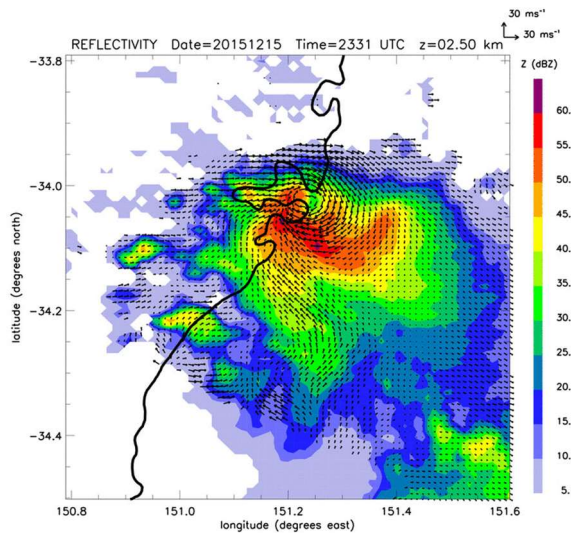

Fig.1 *Observed Radar reflectivity (colours, unit: dBZ) and horizontal winds (arrows, unit: m/s) at 2.5km at 23:31UTC 15 Dec 2015.*

2. Results

The forecasts were carried out using the Regional Atmosphere and Land (RAL) configurations of the Unified Model (UM) developed at the UK Meteorological Office (Bush et. al 2019). The model integrated for 24h with the initial conditions downscaled from the Bureau's global NWP model (ACCESS-G) with a basetime of 15 UTC on 15 December 2015. The model horizontal grid spacing was 1.5 km and there are 90 vertical levels with the highest resolution in the boundary layer. The simulations were using the physics configuration for the middle latitude (RAL2M), and the Tropics (RAL2T). The main differences between RAL2M and RAL2T configurations are the cloud scheme and the boundary layer scheme. We also compared the 1.5 km simulations with additional simulations using a higher horizontal grid spacing of 500m.

Our results showed that the RAL2M model simulation (Fig.2a) was the better simulation in terms of storm track and storm timing. The simulation with RAL2M was able to simulate the rotating winds associated with the storm, which supplied the moisture to further promote the storm's development. The simulated storm reached its maximum rainfall intensity around Kurnell at 01 UTC, 16 Dec 2015, about one hour later than observed. The RAL2T simulations (Fig.2b) failed to produce the convective system along the coast. There was convection initiated at 36.2S close to the coast, but the convection dissipated quickly without further intensification. There were some patches of inland convection developing associated with a trough of low pressure as shown in the weather chart (not shown), which was consistent with the RAL2M experiment.

To understand which differences in model physics between RAL2T and RAL2M caused the different behaviour of convection shown in Fig.2, we carried out two additional RAL2M sensitivity experiments, in which the cloud scheme or the boundary layer scheme were taken from the RAL2T configuration, respectively. Using the boundary layer scheme of RAL2T, the model failed to produce an intensifying storm along the coastline, just like the RAL2T model simulation. This was mainly due to the enhanced mixing in RAL2T that can make it harder to develop the convection. Furthermore, in the RAL2M boundary layer scheme, temperature and moisture perturbations based on surface buoyance flux are included, which helped convection develop over the warm ocean. The RAL2M physics configuration uses a diagnostic cloud scheme, while the RAL2T physics package has a prognostic cloud scheme. Results showed that there was no substantial difference with the initial RAL2M simulation using the prognostic cloud scheme of RAL2T, indicating that the different cloud schemes between RAL2M and RAL2T didn't play an important role in the differences shown in Fig.2. In conclusion, these two experiments clearly demonstrated that the different behaviour observed in Fig.2 can be attributed predominantly to the different boundary layer schemes of the RAL2M and RAL2T configurations.
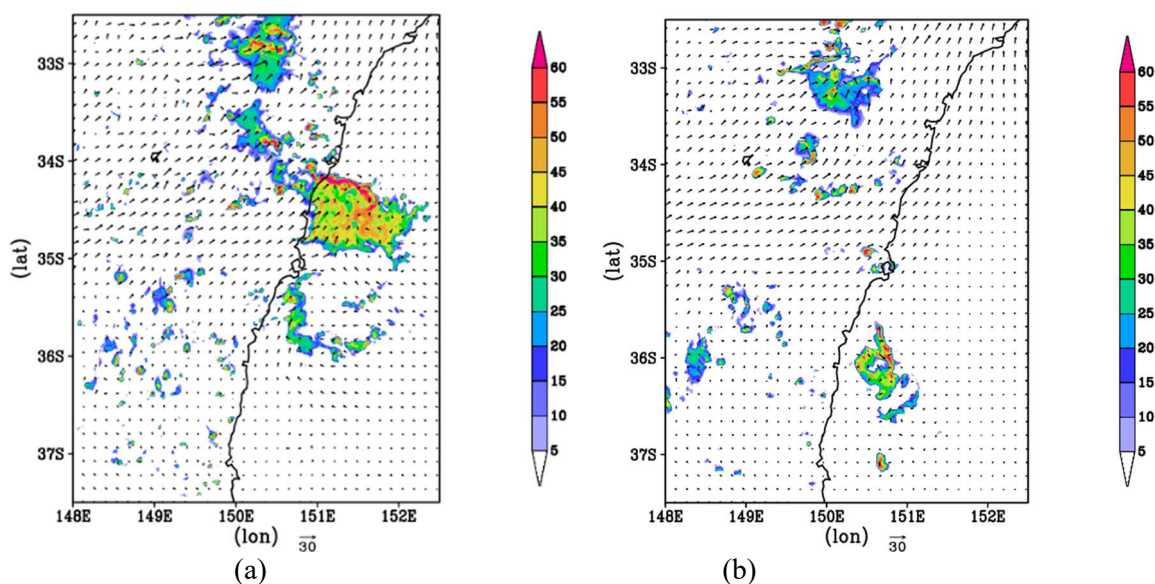
Fig.2 Same as Fig1, but *for the model simulations with 1.5km horizontal resolution (a) using the RAL2M physics package; and (b) using the RAL2T physics package (at 01 UTC, 16 Dec 2015).*

We also conducted an experiment with the RAL2M configuration using a finer horizontal grid length of 500 m instead of 1500m (Fig.3). In this experiment, the simulated storm, in its mature stage, has developed a much stronger cyclonic rotation compared to Fig. 2a with higher wind speeds and higher radar reflectivities (about 12dBZ increase for the maximum), in better agreement with radar observations shown in Fig. 1. In this experiment, the storm reached its mature stage one hour later than that in the 1.5 km RAL2RAL2M simulation presumably due to the slower moving speed for the more intense storm.
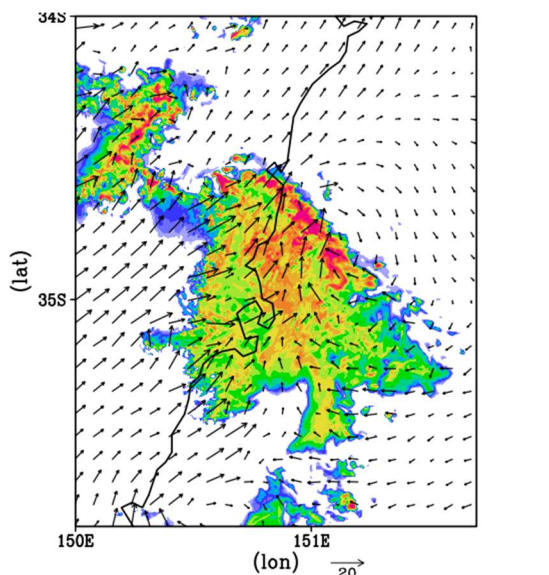

Fig.3, *Same as Fig.1, but for the model experiment using RAL2M physics with 500m horizontal resolution (at 02UTC 16 Dec 2015).*

3. Conclusion

In this study, using the high-resolution UM, we simulated the severe thunderstorm that occurred over the Kurnell peninsula near Sydney on the 15th December 2015. The results show that the model simulation using the middle latitude physics configuration was able to simulate the structure and location of the convective system developing along the coast. In this simulation, the storm also developed rotating winds as observed, which supplied the moisture to further promote the storm's development. In contrast, the simulation with the Tropical configuration failed to simulate the developing convective storm along the coast mainly due to the different boundary layer scheme. Model simulations with 500m resolution further improved the rotating structure of cloud bands but had a tendency to over-estimate the frequency of occurrence of intense rainfall within the storm (not shown).

4. References

Bush, M., and co-authors, 2019: *The first Met Office Unified Model/JULES Regional Atmosphere and Land configuration, RAL1, Geosci. Model Dev. Discuss. https://doi.org/10.5194/gmd-2019-130*